Publications of the Astronomical Society of Australia (2024), **41**, e108, 11 pages
doi:10.1017/pasa.2024.100

CAMBRIDGE UNIVERSITY PRESS

Research Article

WISE J152614.95-111326.4, an unusual variable star

Chris Koen[1] and Alexei Y. Kniazev[2,3]

[1]Department of Statistics, University of the Western Cape, Bellville, Cape, South Africa, [2]South African Astronomical Observatory, Cape, South Africa and [3]Southern African Large Telescope, Observatory, Cape, South Africa

Abstract

New time series photometry of WISE J152614.95-111326.4, an eclipsing binary candidate, has been obtained. Full cycles of variation were covered in five filters, ranging from *B* to *z*. Archival time series photometry is also available from several sources. The phased light curve shape changes from a double wave form in the red, to a single wave at shorter wavelengths. Analysis of the spectral energy distribution and SALT spectra shows the presence of a cool (∼7 250–7 900 K) white dwarf and an M6 star. The light curves can be explained by a hot spot on the opposing hemisphere of the white dwarf. The star may be in a pre-cataclysmic variable phase with a very low rate of mass flow from the red dwarf to the white dwarf, such that no flickering is evident. Evidence in favour of this hypothesis is that the period of the system (2.25 h) is in the cataclysmic variable period gap. It is speculated that a weak magnetic field associated with the white dwarf funnels accreted material onto a magnetic pole. Amplitudes of the *W*1 and *W*2 WISE light curves are anomalously large. The possibility is discussed that variability in this spectral region is primarily driven by electron cyclotron radiation.

Keywords: Stars: binaries: close; stars: variables: general; stars: individual: WISE J152614.95-111326.4

(Received 16 July 2024; revised 28 September 2024; accepted 26 October 2024)

1. Introduction

WISE J152614.95-111326.4 (hereafter WISE 1526-1113) is listed as an eclipsing binary in the Petrosky et al. (2021) catalogue of WISE ('Wide-field Infrared Survey Explorer', Wright et al. 2010) variable stars. It was selected for follow-up photometry as part of a program designed to expand the knowledge base on ultrashort period ($P < 0.2$ d) main sequence (M+M spectral type) binaries (see e.g. Koen 2019, 2022a, 2022c).

It has often been stated in the astronomy literature that there is a lower limit of about 0.2 d to the periods of all contact binaries (e.g. Paczyński et al. 2006). A possible cause is that evolution through angular momentum loss in low mass binaries is so slow that their components cannot fill their Roche lobes within the Hubble time (e.g. Stepień 2006). A contrary view is that angular momentum loss in such binaries is in fact efficient, and contact systems do form, but only if the primary star is massive enough: Jian et al. (2012) found that systems with small primary masses suffer unstable mass transfer which probably leads to overcontact configurations with very short lifetimes. A third scenario invokes the role of distant third components in hierarchical triple systems containing short period binaries. In particular, the period of the inner binary system can be decreased through the amplification of tidal friction by the presence of the distant component (Fabrycky & Tremaine 2007).

More recently Zhang & Qian (2020) and Koen (2022b) used the observed distribution of contact binary periods to derive lower period limits for such systems of 0.148 and 0.08–0.15 d respectively, i.e. somewhat lower than previously assumed.

Study of these issues has been hampered by a dearth of known main sequence binary stars with very short periods. Given the shortness of the periods under consideration, both components of the such binaries are of spectral type M. Being intrinsically faint, and rare, relatively few such systems are known. Koen (2022b) has furthermore pointed out that the rarity of main sequence double stars with $P < 0.2$ d extends to non-contact systems.

WISE 1526-1113 seemed an excellent candidate M+M system, given its extreme period of 0.093796 d and its very red colour (e.g. *Gaia* $B_p - R_p = 2.303$). Nonetheless, follow-up photometry is essential, as many similar systems consist of a red dwarf (RD) and a white dwarf (WD), red colours despite – see e.g. Koen (2022c). Furthermore, in the absence of eclipses, the light curves of the ellipsoidal variations in close binaries can be difficult to discriminate from those of spotted rotators. Lastly, periods determined by large scale surveys are not always reliable (Petrosky et al. 2021; Koen 2022c).

This paper is devoted to a detailed study of WISE 1526-1113, which despite *not* being a main sequence binary, is unusual enough to be of interest. In particular, it will be demonstrated below that the star is comprised of a white dwarf and a red dwarf, with evidence of a low level of mass transfer between the two.

It is noted for later use that the parallax of the star is 8.2795 ± 0.1266 mas (Gaia Collaboration 2023) implying a distance of 120.8 ± 1.8 pc. The Galactic coordinates of WISE 1526-1113 are ($\ell = 352.5167$, $b = 36.3344$).

2. SAAO photometry

Photometric observations were made with CCD cameras mounted on the 1-m and 1.9m telescopes of the South African Astronomical Observatory (SAAO) situated at Sutherland in South Africa. Both cameras have 1 024 × 1 024 pixel imaging areas, and are operated

Corresponding author: Chris Koen; Email: ckoen@uwc.ac.za

Cite this article: Koen C and Kniazev AY. (2024) WISE J152614.95-111326.4, an unusual variable star. *Publications of the Astronomical Society of Australia* **41**, e108, 1–11. https://doi.org/10.1017/pasa.2024.100

Table 1. The photometric observing log. Observing during the first night cycled through the *R* and *I* filters. The SAAO 1.0m telescope was used for the first four runs, and the 1.9m telescope for the last two.

Starting time		Run length	
(HJD 2461000+)	Filters	(h)	*N*
434.3823	*R*,*I*	2.6	40, 43
435.4088	*R*	5.2	118
436.3570	*z*	2.3	77
436.4562	*I*	1.9	155
440.4423	*V*	2.9	69
443.3818	*B*	2.8	66

in frame-transfer mode. Fields of view on the two telescopes are similar – 2.85×2.85 arcmin^2 and 2.79×2.79 arcmin^2 – thanks to a focal reducer being used on the 1.9m telescope.

Sky conditions varied during the observing runs, with some observations obtained through thin clouds. Moonlight phases were dark or grey. Seeing was generally in the range 1–2 arcsec. Exposure times ranged from 40 to 150 s, depending on the filter, telescope and atmospheric conditions. Measurements were obtained through standard BVR_CI_C filters, as well as the Sloan *z* filter. An observing log is given in Table 1.

Reductions were performed using an automated version of DOPHOT (Schechter, Mateo, & Saha 1993). Magnitudes derived from point spread function fitting showed considerably less scatter than those from aperture photometry, and were therefore preferred. Magnitudes were differentially corrected, using a suite of stars in the field of view with constant, low noise light curves.

For convenience the subscripts on the R_C and I_C filternames are dropped in the rest of the paper.

The light curves are plotted in Fig. 1. Several interesting features are evident. First, the shape of the light curve depends strongly on the filter, changing from double waves at *z* and *I* to single waves at *V* and *B*, with *R* being intermediate. Second, the *z* and *I* light curves are very similar. Third, light curves in *V* and *B* appear to have flat maxima. Fourth, amplitudes are wavelength dependent. This will be discussed further in the next section of the paper.

3. Other time series observations

Time series observations of WISE 1526-1113 were obtained as part of the following surveys: WISE[a], ZTF ('Zwicky Transit Facility' – Bellm et al. 2019)[b], CSS ('Catalina Sky Surveys' – Drake et al. 2014)[c] and ATLAS ('Asteroid Terrestrial-impact Last Alert System' – Tonry et al. 2018; Heinze et al. 2018).[d] Use of these data is gratefully acknowledged.

Summary statistics of the datasets are in Table 2, and light curves are plotted in Figs. 2–4. The weighted average of the frequencies extracted from the separate sets of measurements is $f = 10.661333 \pm 2.3 \times 10^{-6}$ d^{-1}. In the cases of the ATLAS *o* and CSS

[a]https://irsa.ipac.caltech.edu/cgi-bin/Gator/nph-scan?submit=Select&projshort=WISE.
[b]https://irsa.ipac.caltech.edu/cgi-bin/Gator/nph-scan?submit=Select&projshort=ZTF.
[c]http://nesssi.cacr.caltech.edu/DataRelease/.
[d]https://fallingstar-data.com/forcedphot/.

Table 2. Statistics of survey time series observations of WISE 1526-1113. The number of observations is denoted by *N*. The last column shows the dominant frequency extracted from each dataset, together with its standard error.

		Start date	Duration		Frequency (uncertainty)
Survey	Filter	(JD 2450000)	(d)	*N*	(d^{-1})
WISE	*W*1	6 700.97	3 448	263	10.661332 (4.1E-6)
WISE	*W*2	6 700.97	3 448	263	10.661328 (6.2E-6)
ATLAS	*o*	7 241.76	3 192	2 387	21.322677 (7.4E-6)
ATLAS	*c*	7 241.75	3 148	771	10.66133 (1.0E-5)
ZTF	*g*	8 203.86	1 971	199	10.66133 (1.7E-5)
ZTF	*r*	8 198.88	1 964	254	10.66131 (2.3E-5)
ZTF	*i*	8 246.77	1 512	62	21.32263 (2.2E-5)
CSS	–	3 525.80	2 926	375	21.32267 (2.0E-5)

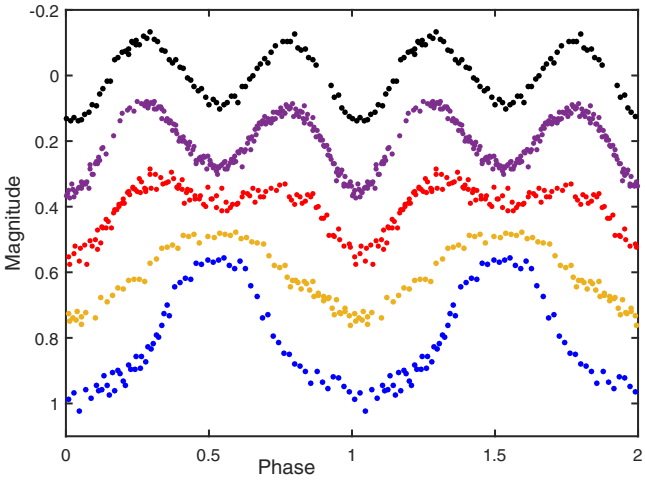

Figure 1. Phase-folded light curves of WISE 1526-113 obtained at SAAO. From top to bottom *z*, *I*,*R*,*V* and *B*. Zeropoints are arbitrary.

data, half the value of the dominant periods were used in the calculation.

The more detailed model

$$Y_\lambda(t) = \mu_\lambda + A_{1\lambda} \cos(2\pi f t + \phi_{1\lambda}) + A_{2\lambda} \cos(4\pi f t + \phi_{2\lambda}) + e_\lambda(t) \quad (1)$$

was next fitted to each of the light curves. In (1), $A_{1\lambda}$ and $A_{2\lambda}$ are the amplitudes of the fundamental frequency *f* and first harmonic $2f$ of variations, with corresponding phases $\phi_{1\lambda}$ and $\phi_{2\lambda}$. The zeropoint is denoted by μ, and noise by $e(t)$. Results are in Table 3, where effective wavelengths of the filters were retrieved from the relevant Spanish Virtual Observatory webpage.[e] Neither A_1 nor A_2 is a monotonic function of wavelength. Perhaps the most striking result is that A_1 is largest for the two infrared wavebands.

4. Spectral Energy Distribution (SED)

Standardised photometry of WISE 1526-113 was collected from the VizieR service of the Strasbourg astronomical Data

[e]http://svo2.cab.inta-csic.es/svo/theory/fps3/.

https://doi.org/10.1017/pasa.2024.100 Published online by Cambridge University Press

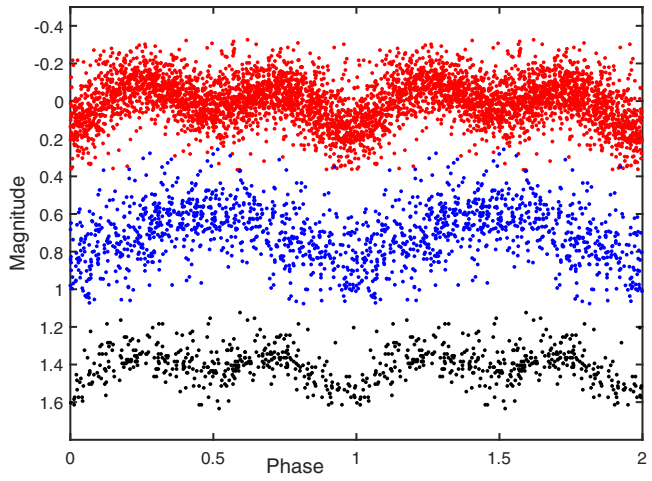

Figure 2. Phased light curves of WISE 1526-1113. From top to bottom ATLAS *o*, ATLAS *c* and CSS. Zeropoints are arbitrary.

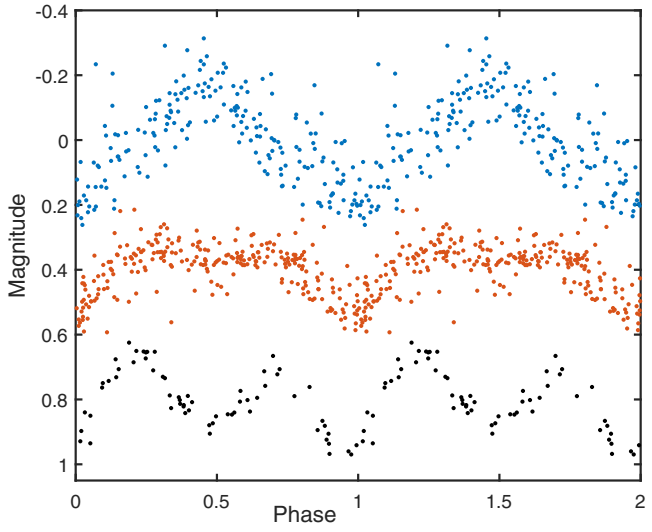

Figure 3. Phased ZTF light curves of WISE 1526-1113. From top to bottom *g*, *r* and *i*. Zeropoints are arbitrary.

Table 3. Amplitudes A_1 and A_2 of the fundamental frequency of variation (10.66133 d^{-1}) and its first harmonic [see Equation (1)]. Standard errors of estimates are given in brackets.

Filter	Effective wavelength (Å)	A_1 (mmag)	A_2 (mmag)
*W*2	46 028	369 (9)	122 (9)
*W*1	33 526	362 (6)	67 (6)
z	8 923	191 (1)	110 (1)
i	7 915	45 (4)	114 (4)
I	7 829	258 (1)	110 (1)
o	6 630	117 (5)	9 (5)
r	6 370	141 (6)	14 (6)
R	6 357	70 (2)	65 (2)
CSS	5 627	46 (4)	65 (4)
V	5 445	126 (2)	7 (2)
c	5 182	51 (2)	76 (2)
g	4 753	64 (3)	47 (3)
B	4 413	206 (3)	45 (3)

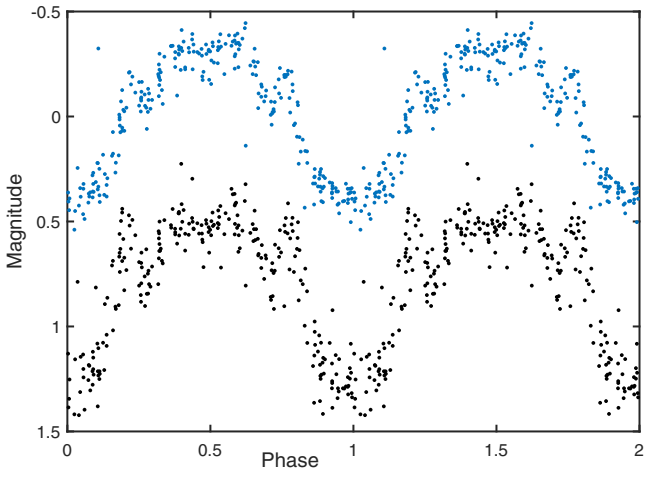

Figure 4. Phased WISE *W*1 (top) and *W*2 (bottom) light curves of WISE 1526-1113. Zeropoints are arbitrary.

Center.[f] Original sources of the data are *Gaia* (Gaia collaboration 2023), Pan-STARRS ('The Panoramic Survey Telescope and Rapid Response System', Chambers et al. 2016), *GALEX* ('Galaxy Evolution Explorer'; Bianchi, Shiao, & Thilker 2017), SkyMapper Southern Sky Survey (Onken et al. 2024), VHS ('VISTA Hemisphere Survey', McMahon et al. 2013), 2MASS ('Two Micron All-Sky Survey', Skrutskie et al. 2006), WISE and the VLT ATLAS survey (Shanks et al. 2015). The efforts of these surveys are gratefully acknowledged.

The field of view of the SAAO 1.9m telescope included two fairly bright stars for which APASS ('AAVSO Photometric All-Sky Survey', Henden et al. 2015) measurements of *B* and *V* are available. These were used to set nightly zeropoints and derive $B = 19.27$ mag and $V = 18.55$ mag. This brings the available number of standardised photometric datapoints to 30.

Spectroscopically it is clear that WISE 1526-1113 has at least two component with widely different colours. One of these appears to be an M dwarf, but the nature of the blue component is not evident from spectra. Clearly, if it is stellar, it must be a cool white dwarf, otherwise its radiation would have been obvious at optical wavelengths. Some insight can be gained by considering colour indices dominated by either component. The IR indices $J - H = 0.88$ and $W1 - W2 = 0.32$, reflecting primarily the SED of the RD, can be matched to those in the tables of Pecaut, Mamajek, & Bubar (2012) and Pecaut & Mamajek (2013)[g]; these suggest spectral types of L2 and L5 respectively. The index $NUV - B = 1.77$, on the other hand, is compatible with a DA white dwarf with T_{eff} ~7 000–8 000 K – see Holberg & Bergeron (2006) and

[f]https://vizier.cds.unistra.fr/viz-bin/VizieR.

[g]http://www.pas.rochester.edu/~emamajek/EEM_dwarf_UBVIJHK_colors_Teff.txt.

https://doi.org/10.1017/pasa.2024.100 Published online by Cambridge University Press

Table 4. Optimal SED models fitted to standardised photometry of WISE 1526-1113, for three assumed values of the reddening $E(B-V)$. Standard errors of estimates are given in brackets. The last column contains the residual standard deviation.

White dwarf properties			Red dwarf properties				
T_{eff} (K)	$\log g$	M_{bol} (mag)	T_{eff} (K)	$\log g$	M_{bol} (mag)	$E(B-V)$ (mag)	σ (mag)
7 405(316)	8.5(1.27)	13.2(0.08)	2 740(33)	5.0(0.46)	10.7(0.06)	0	0.138
7 850(250)	9.5(1.02)	13.0(0.07)	2 770(32)	5.0(0.40)	10.7(0.06)	0.05	0.132
7 970(230)	9.5(0.93)	12.8(0.06)	2 785(33)	5.0(0.75)	10.7(0.06)	0.1	0.126

Bédard et al. (2020).[h] It should be borne in mind though that both measurement errors and intrinsic variability contribute to uncertainties in the photometry. For example, by contrast with the 2MASS $J-H$ index above, the VHS measurement is $J-H=0.63$, which implies a spectral type $\sim M7$.

Starting from

$$L_\lambda = L_0 10^{-0.4M_\lambda}$$

where L_λ and M_λ are the monochromatic luminosity and absolute magnitude,

$$L_{\lambda 1}+L_{\lambda 2} = L_0\left[10^{-0.4M_{\lambda 1}}+10^{-0.4M_{\lambda 2}}\right] \quad (2)$$

where subscripts 1 and 2 refer to the two stars respectively. It follows that the apparent magnitude is

$$\begin{aligned} m_\lambda &= M_\lambda + 5(\log d - 1) \\ &= -2.5\log\left[(L_{\lambda 1}+L_{\lambda 2})/L_0\right] + 5(\log d - 1) \\ &= -2.5\log\left[10^{-0.4(M_{bol1}-BC_{\lambda 1})}+10^{-0.4(M_{bol2}-BC_{\lambda 2})}\right] \\ &\quad +5(\log d - 1) \end{aligned} \quad (3)$$

where d is the distance (in pc) to the stars, and $BC_{\lambda j}$ is the bolometric correction for star j at wavelength λ.

If reddening is included, then the term

$$A_\lambda = f_\lambda R_V E(B-V) \approx 3.1 f_\lambda E(B-V) \quad (4)$$

for the absorption at effective wavelength λ is added to the right-hand side of (3). In (4), $f_\lambda = A_\lambda/A_V$ is conveniently taken from table 3 in Wang & Chen (2019), supplemented by Casagrande et al. (2019) for the SkyMapper filters and Wall et al. (2019) for the *GALEX NUV* band. The ratio of total to selective absorption R_V is assumed to be 3.1 (e.g. Schlafly & Finkbeiner 2011).

A number of interstellar reddening maps have been published recently – see e.g. Capitanio et al. (2017), Green et al. (2018), Chen et al. (2019), Hottier, Babusiaux, & Arenou (2020), Guo et al. (2021), Lallement et al. (2022), Vergely, Lallement & Cox (2022), and references therein. Some of the maps are restricted to the Galactic plane, or have poor resolution (hundreds of parsecs) and are therefore not directly useful. For the distance and direction of WISE 1526-1113 the maps of Capitanio et al. (2017)[i] give $E(B-V)=0.041\pm0.019$ mag, or $A_V=0.13$ mag. The 10 pc resolution G-Tomo reddening maps[j] of Lallement et al. (2022) and Vergely et al. (2022) give a rather smaller value of $A_V=0.050\pm0.001$ mag. These results are consistent with limits on the extinction in the direction of WISE 1526-1113 from Guo et al. (2021) of $E(B-V)\leq 0.11$ mag (for $d\leq 200$ pc) and from Green et al. (2018) of $E(g-r)\leq 0.15$ mag (for $d\leq 300$ pc).

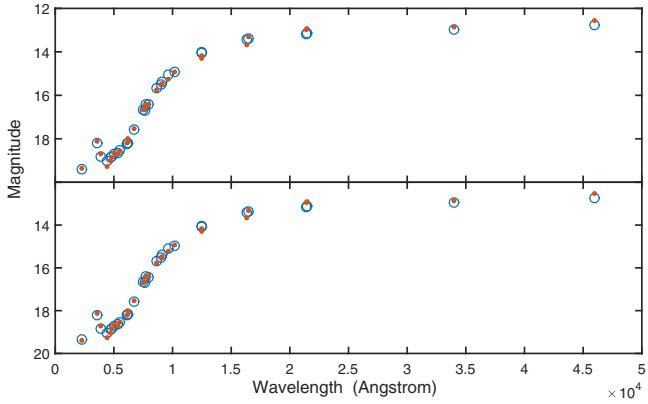

Figure 5. Standardised photometric measurements (dots) compared with predicted magnitudes (open circles) using the Table 4 parameters. The top panel results assume zero reddening, while the bottom panel is based on $E(B-V)=0.1$ mag.

The temperatures and gravities of the two stars are needed to calculate the bolometric corrections. Adding the two bolometric magnitudes, this makes six unknown parameters to be determined when fitting the theoretical SED (3) to the observed photometry. Results are in Table 4, for three assumed values of reddening. Parameter standard errors were calculated by bootstrapping; the uncertainty in the parallax was accommodated by simulating a Gaussian distribution with mean and standard deviation respectively set to the *Gaia* parallax and its error.

In view of the discussion above an assumed reddening of $E(B-V)=0.1$ mag is probably unrealistically large, but it does lead to a slight reduction in the residual standard deviation. The estimated parameter values for the RD differ very little for different values of the reddening, while the estimated WD temperatures and luminosities increase slightly as $E(B-V)$ is increased. A graphical comparison of observed and theoretical magnitudes is presented in Fig. 5; note that all magnitudes have been transformed to the Vega system. It is possible that there is an IR excess at the WISE wavelengths – this could be due to the emission process discussed in Section 8 below. Given the small values of dust absorption predicted by the more accurate reddening maps, and the relatively small improvement in the quality of the model fit when reddening is included, we proceed under the assumption that dust absorption can be ignored.

[h] https://www.astro.umontreal.ca/~bergeron/CoolingModels/.
[i] https://stilism.obspm.fr/.
[j] https://explore-platform.eu/sdas/about/gtomo.

https://doi.org/10.1017/pasa.2024.100 Published online by Cambridge University Press

Table 5. A summary of models fitted to the co-added spectra of WISE 1526-1113. The acronyms 'ET' and 'NGS' represent the 'empirical template' and 'NextGen solar' spectra S_r respectively. Spectra in the former library are given for various spectral types, rather than temperature and gravity. For the solutions in the last two lines the radial velocity was kept fixed at the Hα value. The last column shows the root mean square of the residuals.

				White dwarf properties		Red dwarf properties		
Red spectrum	α	β	V_r (km s^{-1})	T (K)	log ~g	T (K)	log ~g	*RMS*
ET	0.68	0.21	225	7 250	9.5	M6		0.114
NGS	0.56	0.50	196	7 750	9.5	3 000	4.0	0.163
ET	0.68	0.21	225	7 250	9.5	M6		0.114
NGS	0.56	0.50	225	7 750	9.5	3 000	4.0	0.163

5. Southern African Large Telescope (SALT) spectra

We obtained two spectra of WISE 1526−1113 on 2024 May 18 on SALT (Buckley, Swart, & Meiring 2006; O'Donoghue et al. 2006). The observations were carried out with the Robert Stobie Spectrograph (RSS; Burgh et al. 2003; Kobulnicky et al. 2003) in the long-slit mode. Both RSS spectra were taken with a slit width of 1.5 arcsec and with the PG700 grating, which covers the spectral range of 3 650–7 450 Å. This choice of the slit width and grating provides a final reciprocal dispersion of 1.22 Å pixel^{-1} and spectral resolution FWHM of 7.1–7.6 Å ($R \approx 740$). Exposure times were 900 and 1 200 s. An Ar lamp arc spectrum was taken immediately after each science frame and was used for wavelength calibration. The relative flux calibration was performed using observations of spectrophotometric standard stars. Absolute flux calibration is not feasible with SALT because the unfilled entrance pupil of the telescope moves during the observation.

The primary reduction of RSS spectra was performed using the SALT science pipeline (Crawford et al. 2010). For further reduction of the long-slit data we used the RSS pipeline described in detail by Kniazev (2022).

The times of mid-exposure of the two spectra were HJD 2460449.34436 and HJD 2460449.53771, i.e. 4.6404 h apart. This means that the two spectra were obtained at very similar phases (only 6% of a cycle difference). A radial velocity of $V_r = 224.9 \pm 3.3$ km s^{-1} was measured from the Hα emission line.

The co-added spectrum S was modelled by the sum of two spectra, S_w and S_r representing a WD and RD respectively:

$$S(\lambda) = \alpha S_w(\lambda) + \beta S_r(\lambda)\,. \tag{5}$$

The best-fitting combination was determined by performing a grid search over libraries of spectra. Gaussian convolution was used to reduce the resolution of the library spectra to that of the RSS spectrograph (7.3 Å). For each candidate combination two possibilities were entertained – either keeping V_r fixed at the value determined from the strong Hα line, or searching for an optimal value. (Note that this emission line was excluded from the fitting process).

For the WD spectra, a single library source was used[k] – see Tremblay & Bergeron (2009) and Koester (2010) for details. Two sources were used for RD spectral templates – theoretical NextGen solar composition models[l] (Allard et al. 1997; Hauschildt, Allard, & Baron 1999) and empirical templates constructed from SDSS spectra[m] (Kesseli et al. 2017).

The spectral modelling results can be found in Table 5. In order to be able to attach some meaning to the weights α and β in (5), all three spectra were normalised by their respective fluxes at $\lambda =$ 5 550 Å. The last column of the Table contains

$$RMS = \left[\frac{1}{N_\lambda}\sum_\lambda (S - \alpha S_w - \beta S_r)^2\right]^{1/2}\,;$$

it is clear that by this token the empirical template spectra fit the observed spectrum better than the theoretical spectra. According to the Pecaut, Mamajek, & Bubar (2012) and Pecaut & Mamajek (2013)[n] tables, for an M6 dwarf, $T_{eff} = 2\,800$ K, which is in reasonable agreement with the 3 000 K temperature from the NextGen models. The WD spectral properties are very similar across all four models fitted. The agreement between the temperatures derived from SED fitting (first line of Table 4) and those from the spectral fitting using the empirical template is gratifying.

It is also reassuring that the optimal model in the first line of Table 5 recovers the radial velocity measured from the Hα line. The implication is that the emission is associated with the RD, since V_r derived from fitting (5) is determined by the RD spectrum. The fit of the model in the first and third lines of Table 5 is illustrated in Fig. 6.

As a final word, in Fig. 7 the redmost part of the co-added SALT spectra is plotted with the empirical templates for spectral types M4.5 and M6. Allowance has been made for differences in the overall slopes of the spectra. Note that in this case the individual features of the spectra are compared, as is done when spectral type is determined. The M6 template is clearly a far superior match. This provides a fairly accurate reddening-independent estimate of the RD temperature which is in excellent agreement with the SED-derived temperatures in Table 4.

6. Binary star modelling

6.1 Preliminaries

We proceed to model the SAAO photometry by a binary star comprised of a WD with $T_1 = 7\,400$ K and a RD with $T_2 = 2\,740$ K (Table 4). In order to gain a preliminary insight into the system, use is made of fundamental relations between physical quantities.

[k] http://svo2.cab.inta-csic.es/theory/newov2/index.php?models=koester2.
[l] http://svo2.cab.inta-csic.es/theory/newov2/index.php?models=NextGen.
[m] http://svo2.cab.inta-csic.es/theory/newov2/index.php?models=tpl_kesseli.
[n] http://www.pas.rochester.edu/~emamajek/EEM_dwarf_UBVIJHK_colors_Teff.txt.

https://doi.org/10.1017/pasa.2024.100 Published online by Cambridge University Press

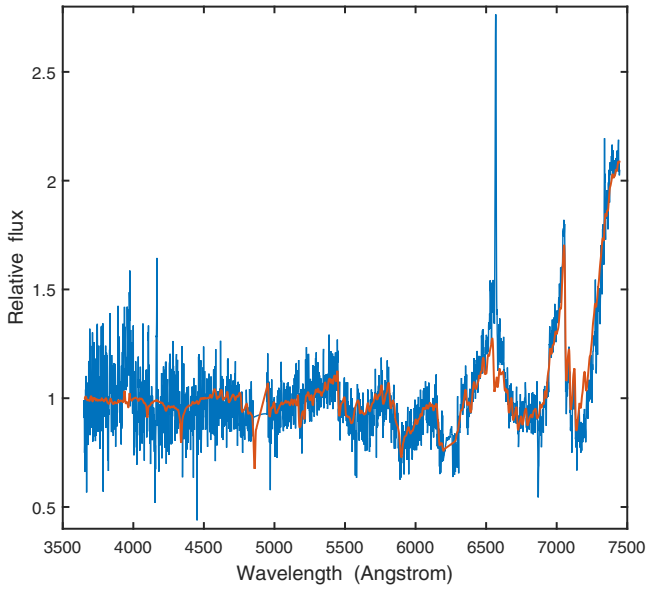

Figure 6. Observed spectrum (blue) and the weighted sum of the best-fitting RD and WD spectra (red).

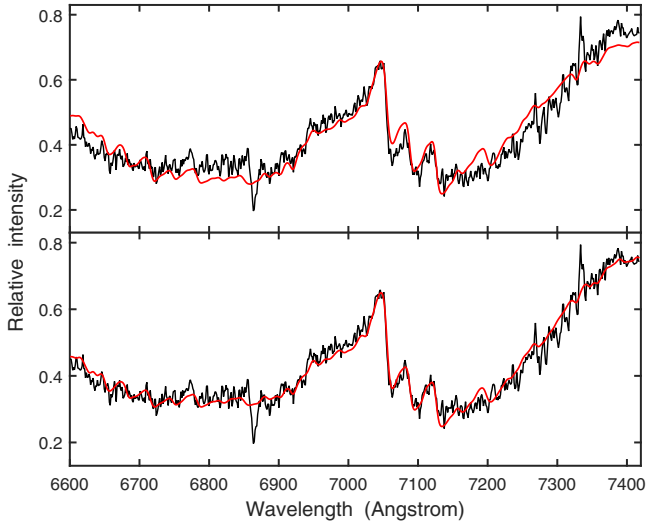

Figure 7. A comparison of the redmost section of the spectrum of WISE 1526-1113 (black) with empirical templatespectra (red), M4.5 in the top panel and M6 in the bottom panel.

First, the radii of the two star follow from

$$L_j/L_\odot = 10^{0.4(4.74-M_{bol,j})} = \frac{R_j^2 T_j^4}{T_\odot^4}$$

where the subscript $j = 1$ for the WD, $j = 2$ for the RD, and the stellar radii are in solar units. The solar bolometric magnitude has been taken as 4.74 mag (Casagrande, Portinari, & Flynn 2006). Therefore,

$$\begin{aligned} R_1 &= 0.0203(T_\odot/T_1)^2 \\ R_2 &= 0.0643(T_\odot/T_2)^2 \end{aligned} \quad (6)$$

where the bolometric magnitudes from the first line of Table 4 have been used. Adopting a solar effective temperature of $T_\odot = 5\,780$ K, $R_1 = 0.0124\,\mathrm{R}_\odot$, and $R_2 = 0.286\,\mathrm{R}_\odot$. Note that adopting the temperatures and bolometric magnitudes in the second line of Table 4 changes these estimates to $R_1 = 0.0121\,\mathrm{R}_\odot$ and $R_2 = 0.280\,\mathrm{R}_\odot$, i.e. minimally different.

The tables of Pecaut, Mamajek, & Bubar (2012) and Pecaut & Mamajek (2013)[o] list 0.13 $\mathrm{R}_\odot$ as a typical radius for an M6 star, i.e. R_2 is about twice the average radius of a single M6 dwarf. In fact, the derived radius of the RD is similar to that of an M4 star, and its bolometric magnitude to that of an M4.5 star. This point will be discussed further in Section 10.

The value of R_1 can be used to estimate the mass of the WD, via e.g. the mass-radius relations in fig. 9 of Parsons et al. (2017), as approximately 0.6 $\mathrm{M}_\odot$. This is close to the mean WD mass of 0.57 $\mathrm{M}_\odot$ in the post-common envelope binary (PCEB) catalogue of Kruckow et al. (2021). The typical mass of an M6 star is 0.1 $\mathrm{M}_\odot$.[p] The expected mass ratio of WISE 1526-1113 is therefore $q \sim 0.17$.

Kepler's third law can be written in the convenient form

$$A = [74.65(M_1 + M_2)P^2]^{1/3} = 0.868(M_1 + M_2)^{1/3} \quad (7)$$

where A is the distance between the two stars (in $R_\odot$); M_1, M_2 are the stellar masses (in $M_\odot$) and P is the period in d. It follows that $A \sim 0.772\,\mathrm{R}_\odot$, and that $r_1 = R_1/A = 0.016$ and $r_2 = 0.371$. This latter value can be compared to the volumetric radius R_0 of the RD's Roche lobe

$$R_0/A = \frac{0.49q^{2/3}}{0.6q^{2/3} + \ln(1 + q^{1/3})} \quad (8)$$

(Eggleton 1983). For $q = 0.17$, $R_0/A = 0.24$, i.e. the estimated RD radius is about 150% the size of its Roche lobe, an unphysical result.

It is therefore apparently not possible to reconcile the RD radius derived from its bolometric magnitude and temperature, with the limit imposed by binary star dimensions (as imposed by Kepler's law and plausible mass ratios). There is little room for manoeuvring – the errors on the estimated temperature and bolometric magnitude are quite small, whereas even for $q = 0.4$, R_0/A is only 0.30.

We therefore choose to proceed with two different models, which are inconsistent with different aspects of the observations. In both cases we accept that $R_2 \approx R_0$, since this eventually leads to binary models which agree reasonably well with the SAAO photometry. It is not clear whether an additional radial velocity study of WISE 1526-1113 will be able to resolve the problem, unless it extends into the ultraviolet, so that velocities of the white dwarf can also measured, and masses of the two components be determined.

The first set of models ('cool models') retains all parameter values determined above, except for R_2. As will be seen below, detailed modelling then suggests $R_2 \sim R_0$, which is, of course, at odds with $M_{bol,2}$ in Table 4. For the second set of models ('hot models') we adopt $T_2 = 3\,100$ K, which is a typical values for a M4.5 star.[q] Note that this is close to the RD temperature estimated from the SALT spectra using the NextGen model spectra. From (6), $R_2 = 0.224\,\mathrm{R}_\odot$ then follows, which is also very similar to the average radius of 0.217 $\mathrm{R}_\odot$ associated with M4.5 stars.[r] As far as the WD is concerned, we adopt $T_1 = 7\,750$ K, again from the NextGen

[o] http://www.pas.rochester.edu/~emamajek/EEM_dwarf_UBVIJHK_colors_Teff.txt.
[p] http://www.pas.rochester.edu/~emamajek/EEM_dwarf_UBVIJHK_colors_Teff.txt.
[q] http://www.pas.rochester.edu/~emamajek/EEM_dwarf_UBVIJHK_colors_Teff.txt.
[r] http://www.pas.rochester.edu/~emamajek/EEM_dwarf_UBVIJHK_colors_Teff.txt.

https://doi.org/10.1017/pasa.2024.100 Published online by Cambridge University Press

solutions in Table 5. From (6), $R_1 = 0.011$ is then obtained. The corresponding WD mass is $M_1 \sim 0.73$, and the resultant mass ratio $q = 0.25$. Equation (8) gives $R_0/A = 0.268$, and with $A = 0.84$ from (7), $R_0 = 0.226$. Note that in this case the model gives the correct bolometric magnitude, and $R_2 \approx R_0$, at the expense of assuming a value of T_2 at odds with the observations.

It is noted that the absence of eclipses of the WD component implies that the system inclination angle is smaller than about 80°.

6.2 Models

Some preliminary modelling of the individual light curves was performed with the BINARY MAKER 3 program.[s] One of the useful features of this software is that it allows models specified in terms of Roche lobe filling factors. Experimentation showed that all viable models had secondary star filling factors close to zero, meaning the RD is close to filling (or slightly overfilling) its Roche lobe.

It is clear from examination of the light curves (with the exception of $W1$ and $W2$) that the secondary minimum at phase 0.5 is progressively filled in by emission as the effective wavelength of the filter decreases. The simplest explanation is the presence of a bright spot (or spots) on the surface of one (or both) of the stars. Experimentation revealed two possibilities: a spot on the side of the RD facing the WD, or a spot on the WD on the surface opposite the RD. Although models with good fits to individual light curves could be obtained with the former alternative, this required different spot temperatures for the different filters. This appears physically possible, if the radiation is non-thermal, but such models are not supported by the binary software packages used. We therefore concentrate on models with a spot on the away-facing hemisphere of the WD, situated at latitude 90°.

Since BINARY MAKER only deals with one light curve at a time the final modelling was done with PyWD2015 (Güzel & Özdarcan 2020), which is an interface for the well known Fortran package originally developed by Wilson & Devinney (1971) (see also Wilson & Van Hamme 2014, and references therein). Model fitting was performed in mode 5, i.e. the binary system was assumed to be semi-detached. The necessary linear limb darkening coefficients were taken from Claret, Hauschildt, & Witte (2012) and Claret et al. (2020), for the RD and WD respectively.

Details of five illustrative models are given in Table 6. Flux light curves were used, normalised to unity at maximum, hence the residual standard deviations (calculated from the combined residuals in all filters) are dimensionless. We emphasise that the intention is to demonstrate the feasibility of the models, rather than attempt to determine definitive parameter values – the available observations simply cannot constrain all the physical properties of the system, as is clear from the diversity of the models which all fit the data quite well.

The fit of the first model is illustrated in Fig. 8. On the scale of the figure, light curves for the other four models are virtually indistinguishable from those plotted. Clearly the system parameters cannot be definitively determined from the photometry: in particular, there is no guarantee that any model is *globally* optimal.

The first three models were calculated with T_1 and T_2 fixed at the values determined from the SED fitting, but differ primarily in the properties of the spot models. The last two models were calculated with larger values of T_1 and T_2. As expected, M_{bol2} for the higher temperature models is closer to the values in Table 4, but still significantly too large.

Also in Table 6 are the predicted velocity semi-amplitudes

$$K_1 = \frac{2\pi A q}{(1+q)P} \sin i$$

$$K_2 = \frac{2\pi A}{(1+q)P} \sin i\,.$$

[s] http://binarymaker.com.

Table 6. Parameters of five models fitted to the SAAO photometry of WISE 1526-1113. The symbols T_s, R_s and σ respectively denote the temperature and radius of the hot spot, and the standard deviation of the model fit residuals. In all cases the spot is located at longitude 180°.

	Cool models			Hot models	
T_1 (K)	7 400	7 400	7 400	7 750	7 643
T_2 (K)	2 740	2 740	2 740	3 100	3 100
R_1 ($R_\odot$)	0.0119	0.0119	0.0118	0.018	0.018
R_2 ($R_\odot$)	0.170	0.165	0.144	0.189	0.184
R_0 ($R_\odot$)	0.223	0.215	0.189	0.227	0.221
M_1 ($M_\odot$)	0.617	0.624	0.6488	0.794	0.803
M_2 ($M_\odot$)	0.080	0.072	0.047	0.110	0.101
q	0.129	0.115	0.073	0.139	0.126
M_{bol1} (mag)	13.31	13.31	13.31	12.20	12.26
M_{bol2} (mag)	11.83	11.91	12.2	11.07	11.13
b (deg)	90	90	57.8	90	90
T_s (K)	9 420	11 410	9 175	10 040	9 850
R_s (deg)	32.2	20.7	32.2	32.2	32.2
i (deg)	65.3	65.9	67.8	70.0	70
A ($R_\odot$)	0.77	0.77	0.77	0.84	0.84
K_1 (km s^{-1})	43	39	26	52	48
K_2 (km s^{-1})	334	343	358	374	378
σ	0.018	0.013	0.021	0.019	0.018

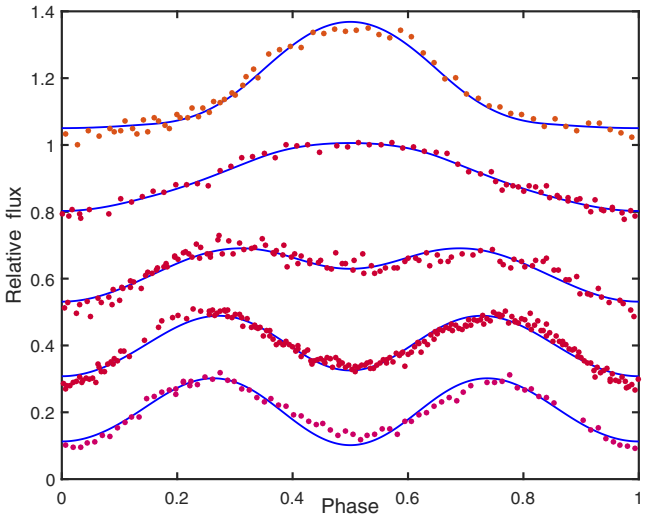

Figure 8. Theoretical (lines) and observed (dots) light curves of WISE 1526-1113. Parameters of the model are in the first column of Table 6. From top to bottom, *B*, *V*,*R*, *I* and *z*. The zeropoints of the normalised fluxes have been shifted for ease of plotting.

https://doi.org/10.1017/pasa.2024.100 Published online by Cambridge University Press

Provided the inclination angle can be determined with reasonable certainty, it may be possible to use measurement of K_2 to discriminate between hot and cold models.

7. Evolutionary state

Given that the WD component has evolved beyond its main sequence life, and given the very short period of the system, WISE 1526-1113 is evidently a PCEB. A common class of PCEBs comprising a WD–RD pair is the cataclysmic variables (CVs). In CVs, the RD fills its Roche lobe and transfers mass to its compact companion. In the case of WISE 1526-1113 the absence of short-timescale stochastic variability ('flickering') in the SAAO photometry, and the absence of emission aside from Hα, imply that the star does not show overt signs of mass transfer. It is therefore of interest to consider how it fits into the general scheme of PCEB and CV evolution. The discussion below draws on descriptions in the papers by Ritter (2012), Liu et al. (2023), Schreiber, Belloni, & Schwope (2024), and references therein.

Evolution of PCEBs proceeds by angular momentum loss. In the initial configuration the cool star (donor) fills its Roche lobe. A magnetic field associated with this donor exerts a torque on the binary system, reducing the period from several hours to ∼3 h. At this point, the donor becomes fully convective, and shrinks, so that the system becomes detached. The efficiency of magnetic braking is reduced, and angular momentum loss is driven by gravitational radiation. This situation persists until the binary orbit has shrunk sufficiently (period ∼2 h) for the donor to once again fill its Roche lobe, enabling mass transfer to resume. The range 2–3 h is often referred to as the 'period gap': observationally, there is a dearth of CVs with periods in this range.

It is noteworthy that the period of WISE 1526-1113 (2.25 h) lies in the period gap. We speculate that the star is currently close to being in a semi-detached configuration, with an orbit which will shrink until mass transfer resumes when the period has decreased to about 2 h More specifically, we posit that WISE 1526-1113 is in a state similar to the well known RD+WD system QS Vir, in which a low level of mass transfer ($\sim 10^{-16}$–10^{-13} $M_\odot$ yr^{-1}) is thought to be taking place, despite its apparently detached configuration (e.g. Matranga et al. 2012; Drake et al. 2014). Other pre-CVs with low accretion rates are described by Schmidt et al. (2007), Tappert et al. (2011) and Longstaff et al. (2019).

A possible explanation for the presence of a hot spot on the surface of the WD is funnelling of accreted material onto a magnetic pole, as happens in polars (e.g. Cropper 1990). At first glance this appears to be backed up by the detection of X-ray emission from the system (by the eROSITA survey – Merloni et al. 2024). The X-ray flux measurements made by the mission are discussed in more detail in Freund et al. (2024) and Schwope et al. (2024). WISE 1526-113 has an entry in the Freund et al. (2024) catalogue of coronal X-ray sources, but is flagged as having 'properties untypical for coronal X-ray emitters'. This designation is used for sources which either have anomalously strong X-ray emission, or lie more than 1.5 mag below the $M_G - (B_p - R_p)$ main sequence. In the case of WISE 1526-113, the latter condition applies – this appears to be due primarily to its anomalously blue $B_p - R_p$ index, which suggests a spectral type ∼M2, for which $M_G \sim 9.3$, compared with $M_G \sim 12.0$ for an M4.5 star[†] (and $M_G = 12.1$ for WISE 1526-1113). In other words, the RD component is probably *not* an untypical coronal X-ray source – its peculiar position in the colour–magnitude diagram is simply due to its composite nature. Furthermore, the characteristic temperatures seen in even low accretion rate polars are far in excess of those derived for WISE 1526-1113 (e.g. Schwope et al. 2002).

It has been noted in the literature that RDs in pre-CVs may be overluminous, due to inflated radii. This has been ascribed to the stars being out of thermal equilibrium, following the stage of common-envelope evolution (e.g. Schreiber & Gänsicke 2003). The phenomenon has been seen in a number of relatively young pre-CVs (Sing et al. 2004), and could contribute to the large value of R_2 derived in Section 6.1.

8. The WISE light curves

Given that the accreted mass in the WISE 1526-1113 system appears to arrive in a limited area on the WD surface, which is furthermore on the side opposite the RD, it seems likely that there is at least a modest magnetic field associated with the WD. It is therefore reasonable to consider a non-thermal source for the large amplitude variability seen in the WISE $W1$ and $W2$ bands, which cannot be explained by the models in Section 6. We hypothesise that the light curves in Fig. 4 are the result of electron cyclotron radiation near or at a magnetic pole of the WD, similar to what is seen in polars (e.g. Harrison & Campbell 2015; Liu et al. 2023). One piece of evidence in favour of this notion is that the maxima in the $W1$ and $W2$ light curves occur at the same phase as the maximum in B, i.e. presumably when the accretion spot is most visible. We also note that the peak-to-peak amplitudes are ∼1 mag in both filters, very similar to what is seen in the low mass polar CSS 1603+19 (Liu et al. 2023).

The electron cyclotron spectrum is described by

$$\lambda_n = \frac{2\pi m_e c^2}{nBq} = \frac{1.0711 \times 10^8}{nB} \quad (9)$$

(e.g. Liu et al. 2023), where the magnetic field strength B is in Gauss, and the wavelength λ_n of radiation in micron. In (9), m_e and q are the electron mass and charge, and c is the speed of light (all in CGS units); n is the harmonic number. This implies that λ_2 and λ_3 are comfortably in the $W2$ and $W1$ bandpasses if $B = 11 - 12$ MG. For $B = 6$ MG, λ_4 and λ_5 are in the ranges of the two filters. For $B = 3$ MG, the $n = 8$ and $n = 10$ harmonics lie in the $W2$ and $W1$ bandpasses.

We close this section with a few additional remarks:

(i) The accretion rate in WISE 1526-1113 is probably quite low. This would imply that low harmonics of cyclotron radiation are optically thin, and hence observable in principle (Harrison & Campbell 2015).

(ii) If cyclotron radiation is the correct explanation for the anomalously large amplitudes in Fig. 4, then JHK light curves could help to constrain the magnetic field strength.

(iii) Close inspection of Fig. 4 reveals that there may be additional structure in the IR light curves – note the dips near phases 0.27 and 0.72. A possible explanation is obscuration by an accretion stream.

(iv) The large amplitudes of variations in $W1$ and $W2$ obviously affect the accuracy of the WISE photometry plotted

[†] http://www.pas.rochester.edu/∼emamajek/EEM_dwarf_UBVIJHK_colors_Teff.txt.

https://doi.org/10.1017/pasa.2024.100 Published online by Cambridge University Press

Table 7. Optimal SED models fitted to standardised photometry of three stars with light curves resembling those of WISE 1526-1113. Standard errors of estimates are given in brackets. The penultimate column gives the number of photometric measurements taken into account, and the last column contains the residual standard deviation. The last line of the Table illustrates the effect of excluding the *GALEX NUV* measurement of ATO J218.9548-17.7890.

Star	White dwarf properties			Red dwarf properties				
	T_{eff} (K)	log g	M_{bol} (mag)	T_{eff} (K)	log g	M_{bol} (mag)	n	σ (mag)
TIC 36077464	25 000(5290)	8.5(0.7)	9.6(0.5)	3 395(35)	4.7(0.6)	8.66(0.02)	19	0.045
ATO J041.1519-14.9620	13 995(9833)	9.5(1.4)	13.02(0.6)	3 305(28)	4.7(0.4)	8.93(0.02)	21	0.043
ATO J218.9548-17.7890	6 850(241)	9.5(0.7)	14.1(0.1)	3 070(39)	4.0(0.4)	10.93(0.03)	19	0.047
	8 475(2264)	9.5(1.0)	14.1(0.3)	3 055(36)	5.0(0.5)	10.93(0.03)	18	0.039

in Fig. 5. It is therefore not clear if the apparent excesses at 3.4 and 4.6 μm are real; if they are, then cyclotron radiation is a promising candidate for their origin.

9. Stars with similar optical light curves

Koen (2022c) found three binary stars in which the light curve morphologies change with wavelength similarly to what is seen in WISE 1526-1113 – see figs. 4 (TIC 36077464), 6 (ATO J041.1519-14.9620) and 14 (ATO J218.9548-17.7890) in that paper. The periods of the stars are short – 4.1, 2.3 and 4.4 hr respectively. Koen (2022c) assumed that these are RD+RD systems, but noted that one of the stars – TIC 36077464 – showed an excess of flux at short optical wavelengths. Here we explore the possibility that these are actually WD+RD pairs, by fitting SEDs to the available standardised photometry, in the manner of Section 4.

Photometry from the sources mentioned in Section 4 are used, except that we do not include VISTA measurements. For reasons which are not obvious the photometry from the latter source is highly discrepant with the rest. As an example, for TIC 36077464, VISTA $K_S = 10.43$ compared to 2MASS $K_S = 9.44$, the latter being perfectly compatible with the remainder of the measurements for that star. The estimated reddening for the stars lies in the range $0.001 \leq E(B-V) \leq 0.009$ mag (Capitanio et al. 2017) and will therefore be ignored.

The results can be seen in Table 7. With the exception of ATO J218.9548-17.7890, the temperatures of the WD components are very uncertain. The last line of the Table provides an explanation of the success of the ATO J218.9548-17.7890 model – the availability of a *NUV* measurement. Evidently this is very useful in constraining the temperature of the WD component due to the steep slope of the SED in this wavelength range. Unfortunately there are no *GALEX* measurements of the other two stars.

All three stars are included in the Freund et al. (2024) catalogue of coronal X-ray sources detected by eROSITA. TIC 36077464 and ATO J041.1519-14.9620 are classified as typical coronal emitters, while ATO J218.9548-17.7890 is flagged as an 'untypical' source. As for WISE 1526-1113, this is not due to the star being X-ray luminous, but because it lies below the main sequence in an HR diagram (as expected for a RD with a blue excess due to a WD companion).

It is noted in passing that TIC 36077464 and ATO J041.1519-14.9620 were also detected by ROSAT (Boller et al. 2016; Freund et al. 2022), and TIC 36077464 by the XMM-Newton survey (Freund et al. 2018).

In conclusion, it is possible that all three systems discussed in this section are also low accretion rate pre-CVs. This is especially likely in the case of ATO J218.9548-17.7890, which has properties quite similar to those of WISE 1526-1113, and a period of 2.3 which also places it in the CV period gap.

10. Discussion

The contents of Section 6 demonstrate that a range of binary models give reasonable fits to the photometric observations. However, the models fail to account for the large luminosity derived from the *Gaia* parallax of the star. The evidence presented above suggests that the RD fills its Roche lobe and that there is likely to be some transfer of mass to the WD component. This could explain the anomalously large value of R_2 we derive – as mentioned by e.g. Nelson et al. (2018), donor components may not be in thermal equilibrium, leading to bloating. Put differently, given the PCEB nature of the star, it is not surprising that the radius, luminosity, mass, and temperature are not all in agreement with any one main sequence spectral type.

Two other points may be worth mentioning. The first is that if a second RD component, with SED close to an M6 spectra, were to be part of the in WISE 1526-1113 system, it would go some way towards explaining the apparent luminosity excess of the system. Second, if the mass of the RD were considerably larger than suggested by its spectral type, then R_2/R_0 would be decreased, i.e. the discrepancy between the size of the RD and its Roche lobe would diminish. To see this, note that by combining (7) and (8), and assuming $M_1 = 0.6 M_\odot$ and $R_2 = 0.286\ \mathrm{R}_\odot$,

$$R_0/R_2 = \frac{0.36 q^{2/3}(1+q)^{1/3}}{0.6 q^{2/3} + \ln(1+q^{1/3})} \tag{14}$$

Fig. 9 shows the dependence of this ratio on the mass ratio q. As an example, $R_2 = R_0$ for $q = 0.6$ (i.e. $M_2 = 0.36\ \mathrm{M}_\odot$, the mass of an M3V star).[u]

A number of additional observations of WISE 1526-1113 would be useful. Further spectra of the star, covering shorter wavelengths, could help to further constrain the nature of the WD component. Of course, given the B filter magnitude of 19.3, this would probably require observing time on a 10m class telescope, or from space in the UV. A more direct route to establishing stellar masses, or at least the mass ratio, would be through a radial velocity study. Time series photometry in the *YJHK* bands would

[u] http://www.pas.rochester.edu/~emamajek/EEM_dwarf_UBVIJHK_colors_Teff.txt.

https://doi.org/10.1017/pasa.2024.100 Published online by Cambridge University Press

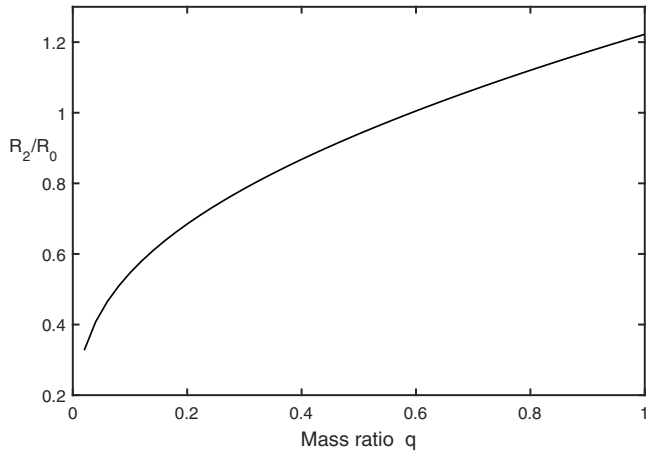

Figure 9. The ratio of the radius R_2 of the RD to the radius R_0 of its Roche lobe, as a function of the mass ratio M_2/M_1.

help to establish the wavelengths at which the variability amplitude is large compared to that in the optical, which again would help constrain the source of the variable IR radiation, and possibly the magnetic field strength. Time series polarisation observations could provide information about the strength and configuration of magnetic fields in the star system.

Acknowledgement. Allocation of telescope time by the South African Astronomical Observatory and the Southern African Large Telescope is acknowledged. The authors are particularly grateful for Director's Discretionary Time awarded in order to obtain SALT spectra of WISE 1526-1113. This research has made use of the VizieR catalogue access tool and the Simbad Astronomical Database at CDS, Strasbourg, France; the collection of stellar model spectra and filter transmission functions of the Spanish Virtual Observatory;[v] bolometric corrections from the "MESA Isochrones and Stellar Tracks";[w] and the results of various large photometric surveys referred to in sections 3 and 4 of the paper. The creators of the PyWD2015 interface have performed a commendable service. A.K. acknowledges support from the National Research Foundation (NRF) of South Africa. Comments by the referee led to considerable improvements in the paper.

Data availability statement. SAAO photometry is available from the first author, and the SALT spectra from the second author. Other data can be obtained from sources given in the text.

References

Allard, F., Hauschildt, P. H., Alexander, D.R., & Starrfield, S. 1997, ARA&A, 35, 137
Bédard, A., Bergeron, P., Brassard, P., & Fontaine, G. 2020, ApJ, 901, 93
Bellm, E. C., et al. 2019, PASP, 131, 018002
Bianchi, L., Shiao, B., & Thilker, D. 2017, ApJS, 230, 24
Boller, Th., Freyberg, M. J., Trümper, J., Haberl, F., Voges, W., & Nandra, K. 2016, A&A, 588, A103
Borowicz, et al. 2023, AcA, 73, 265
Buckley, D. A. H., Swart, G. P., & Meiring, J. G. 2006, Proc. SPIE, 6267, 32
Burgh, E. B., Nordsieck, K. H., Kobulnicky, H. A., Williams, T. B., O' Donoghue, D., Smith, M. P., & Percival, J. W. 2003, Proc. SPIE, 4841, 1463
Capitanio, L., Lallement, R., Vergely, J.L., Elyajouri, M., & Monreal-Ibero, A. 2017, A&A, 606, A65
Casagrande, L., Portinari, L., & Flynn, C. 2006, MNRAS, 373, 13
Casagrande, L., Wolf, C., Mackey, A. D., Nordlander, T., Yong, D., & Bessell, M. 2019, MNRAS, 482, 2770
Chambers, K. C., et al. 2016, arXiv:1612.05560
Chen, B.-Q., et al. 2019, MNRAS, 483, 4277
Claret, A., Cukanovaite, E., Burdge, K., Tremblay, P.-E., Parsons, S., & Marsh, T. R. 2020, A&A, 634, A93
Claret, A., Hauschildt, P. H., & Witte, S. 2012, A&A, 546, A14
Crawford, S. M., et al. 2010, in Proceedings of SPIE Conference Series, Vol. 7737, Observatory Operations: Strategies, Processes, and Systems III, ed. D. R. Silva, A. B. Peck, & B. T. Soifer (Bellingham: SPIE), 773725
Cropper, M. 1990, SSRv, 54, 195
Drake, A. J., et al. 2014, ApJS, 213, 9
Eggleton, P. P. 1983, ApJ, 268, 368
Fabrycky, D., & Tremaine, S. 2007, ApJ, 669, 1298
Freund, S., et al. 2024, A&A, 684, A121
Freund, S., Czesla, S., Robrade, J., Schneider, P. C., & Schmitt, J. H. M. M. 2022, A&A, 664, A105
Freund, S., Robrade, J., Schneider, P. C., & Schmitt, J. H. M. M. 2018, A&A, 614, A125
Gaia Collaboration 2023, A&A, 674, A1
Green, G. M., et al. 2018, MNRAS, 478, 651
Guo, H.-L., et al. 2021, ApJ, 906, 47
Güzel, O., & Özdarcan, O. 2020, CoASka, 50, 535
Harrison, T. E., & Campbell, R. K. 2015, ApJS, 219, 32
Hauschildt, P. H., Allard, F., & Baron, E. 1999, ApJ, 512, 377
Heinze, A. N., et al. 2018, AJ, 156, 241
Henden, A. A., Levine, S., Terrell, D., & Welch, D. L. 2015, AAS, 225, id.336.16
Holberg, J. B., & Bergeron, P. 2006, AJ, 132, 1221
Hottier, C., Babusiaux, C., & Arenou, F. 2020, A&A, 641, A79
Jiang, D., Han, Z., Ge, H., Yang, L., & Li, L. 2012, MNRAS, 421, 2769
Kesseli, A. Y., West, A. A., Veyette, M., Harrison, B., Feldman, D., & Bochanski, J. J. 2017, ApJS, 230, 16
Kniazev, A. V. 2022, AstBu, 77, 334
Kobulnicky, H. A., Nordsieck, K. H., Burgh, E. B., Smith, M. P., Percival, J. W., Williams, T. B., & O'Donoghue, D. 2003, Proc. SPIE, 4841, 1634
Koen, C. 2019, MNRAS, 490, 1283
Koen, C. 2022a, MNRAS, 510, 1857
Koen, C. 2022b, MNRAS, 513, 1526
Koen, C. 2022c, MNRAS, 516, 2540
Koester, D. 2010, MemSAI, 81, 921
Kruckow, M. U., Neunteufel, P. G., Di Stefano, R., Gao, Y., & Kobayashi, C. 2021, ApJ, 920, 86
Lallement, R., Vergely, J. L., Babusiaux, C., & Cox, N. L. J. 2022, A&A, 661, A147
Liu, Y., Hwang, H.-C, Zakamska, N., & Thorstensen, J. R. 2023, MNRAS, 522, 2719
Longstaff, E. S., Casewell, S. L., Wynn, G. A., Page, K. L., Williams, P. K. G., Braker, I., & Maxted, P. F. L. 2019, MNRAS, 484, 2566
Matranga, M., Drake, J. D., Kashyap, V., & Steeghs, D. 2012, ApJ, 747, 132
McMahon, R. G., Banerji, M., Gonzalez, E., Koposov, S. E., Bejar, V. J., Lodieu, N., Robolo, R., & VHS Collaboration 2013, Msngr, 154, 35
Merloni, A., et al. 2024, A&A, 682, A34
Nelson, L., Schwab, J., Ristic, M., Rappaport, S. 2018, ApJ, 866, 88
O'Donoghue, D., et al. 2006, MNRAS, 372, 151
Onken, C. A., Wolf, C., Bessell, M. S., Chang, S.-W., Luvaul, L. C., Tonry, J. L., White, M. S., & Da Costa, G. S. 2024, PASA, 41, 61
Paczyński, B., Szczygieł, D. M., Pilecki, B., & Pojmański G. 2006, MNRAS, 368, 1311
Parsons, S. G., et al. 2017, MNRAS, 470, 4473
Pecaut, M. J., & Mamajek, E. E. 2013, ApJS, 208, 9
Pecaut, M. J., Mamajek, E. E., & Bubar, E. J. 2012, ApJ, 746, 154
Petrosky, E., Hwang, H.-C., Zakamska, N. L., Chandra, V., & Hill, M. J. 2021, MNRAS, 503, 3975
Ritter, H. 2012, MmSAI, 83, 505
Schechter, P. L., Mateo, M., & Saha, A. 1993, PASP, 105, 1342

[v] http://svo2.cab.inta-csic.es/theory/main/.
[w] http://waps.cfa.harvard.edu/MIST/model_grids.html#bolometric/.

https://doi.org/10.1017/pasa.2024.100 Published online by Cambridge University Press

Schlafly, E. F., & Finkbeiner, D. P. 2011, ApJ, 737, 103
Schmidt, G. D., Szkody, P., Henden, A., Anderson, S. F., Lamb, D. Q., Margon, B., & Schneider, D. P. 2007, ApJ, 654, 521
Schreiber, M. R., Belloni, D., & Schwope, A. D. 2024, A&A, 682, L7
Schreiber, M. R., & Gänsicke, B. T. 2003, A&A, 406, 305
Schwope, A., et al. 2024, A&A, 686, A110
Schwope, A. D., Brunner, H., Hambaryan, V., Schwarz, R., Staude, A., & Szokoly, G. 2002, in The Physics of Cataclysmic Variables and Related Objects, ASP Conference Series, ed. B. T. Gänsicke, K. Beuerman, K. Reinsch, 261, 102
Shanks, T., et al. 2015, MNRAS, 451, 4238
Sing, D. K., et al. 2004, AJ, 127, 2936
Skrutskie, M. F., et al. 2006, AJ, 131, 1163
Stepień, K. 2006, AcA, 56, 347
Tappert, C., Gänsicke, B. T., Schmidtobreick, L., & Ribeiro, T. 2011, A&A, 532, A129
Tonry, J. L., et al. 2018, PASP, 130, 064505
Tremblay, P.-E., & Bergeron, P. 2009, ApJ, 696, 1755
Vergely, J. L., Lallement, R., & Cox, N. L. J. 2022, A&A, 664, A174
Wall, E. E., Kilic, M., Bergeron, P., Rolland, B., Genest-Beaulieu, C., & Gianninas, A. 2019, MNRAS, 489, 5046
Wang, S., & Chen, X. 2019, ApJ, 877, 116
Wilson, R. E., & Devinney, E. J. 1971, ApJ, 166, 605
Wilson, R. E., & Van Hamme, W. 2014, ApJ, 780, 151
Wright, E. L., et al. 2010, AJ, 140, 1868
Zhang, X.-D., & Qian, S.-B. 2020, MNRAS, 497, 3493

https://doi.org/10.1017/pasa.2024.100 Published online by Cambridge University Press